(28) (Fig. 5B). Bone development was visualized in whole embryos by Alizarin Red S staining (Fig. 5C), along with hematoxylin-and-eosin staining of thin sections (Fig. 5D). In control animals, extensive skeletal development was evident in the cranial and pharyngeal region at 8 dpf. No bone formation was observed in any of the TAZ-depleted embryos at 8 dpf, the latest time point we could observe before embryonic death. These findings confirm a critical role for TAZ in osteoblast differentiation in vivo. We are unable to comment on the role of TAZ in adipogenesis in these embryos, because adipocytes have not been described in teleosts (although they presumably exist), and in other vertebrate species, fat deposition does not occur until the postnatal period (23).

One function of TAZ is as a transcriptional modifier of mesenchymal stem cell differentiation by promoting osteoblast differentiation while simultaneously impairing adipocyte differentiation, as we have shown (Fig. 5E). Differentiation of MSCs into osteoblasts is critically dependent on Runx2 (4, 5). Our findings implicate TAZ in this process: (i) TAZ functions as an endogenous coactivator of Runx2 in cells; (ii) stimuli that promote bone formation tran-scriptionally up-regulate TAZ concurrently with Runx2; and (iii) TAZ-deficient zebrafish embryos are defective in bone formation. In contrast, stem cell differentiation into adipocytes requires PPARγ-dependent transcriptional events that are directly inhibited by endogenous TAZ. Thus, TAZ may act as a molecular rheostat to fine-tune the balance between osteoblast and adipocyte development.

References and Notes

1. M. F. Pittenger et al., Science 284, 143 (1999).
2. A. I. Caplan, S. P. Bruder, Trends Mol. Med. 7, 259 (2001).
3. P. Ducy, R. Zhang, V. Geoffroy, A. L. Ridall, G. Karsenty, Cell 89, 747 (1997).
4. T. Komori et al., Cell 89, 755 (1997).
5. F. Otto et al., Cell 89, 765 (1997).
6. P. Tontonoz, E. Hu, B. M. Spiegelman, Cell 79, 1147 (1994).
7. E. D. Rosen et al., Mol. Cell 4, 611 (1999).
8. K. Nakashima, B. de Crombrugghe, Trends Genet. 19, 458 (2003).
9. E. D. Rosen, C. J. Walkey, P. Puigserver, B. M. Spiegelman, Genes Dev. 14, 1293 (2000).
10. P. Meunier, J. Aaron, C. Edouard, G. Vignon, Clin. Orthop. 80, 147 (1971).
11. R. Burkhardt et al., Bone 8, 157 (1987).
12. O. Kajkenova et al., J. Bone Miner. Res. 12, 1772 (1997).
13. S. Verma, J. H. Rajaratnam, J. Denton, J. A. Hoyland, R. J. Byers, J. Clin. Pathol. 55, 693 (2002).
14. M. E. Nuttall, J. M. Gimble, Bone 27, 177 (2000).
15. F. S. Kaplan, E. M. Shore, J. Bone Miner. Res. 15, 2084 (2000).
16. D. J. Prockop, Science 276, 71 (1997).
17. S. C. Chang et al., J. Surg. Res. 119, 85 (2004).
18. F. Kanai et al., EMBO J. 19, 6778 (2000).
19. C. B. Cui, L. F. Cooper, X. Yang, G. Karsenty, I. Aukhil, Mol. Cell. Biol. 23, 1004 (2003).
20. R. Yagi, L. F. Chen, K. Shigesada, Y. Murakami, Y. Ito, EMBO J. 18, 2551 (1999).
21. T. Katagiri et al., J. Cell Biol. 127, 1755 (1994).
22. S. Gallea et al., Bone 28, 491 (2001).
23. P. Cornelius, O. A. MacDougald, M. D. Lane, Annu. Rev. Nutr. 14, 99 (1994).
24. Y. Barak et al., Mol. Cell 4, 585 (1999).
25. N. Kubota et al., Mol. Cell 4, 597 (1999).
26. Z. Wu et al., Mol. Cell 3, 151 (1999).
27. Y. Tian, T. Benjamin, unpublished observations.
28. J.-H. Hong, N. Hopkins, M.B. Yaffe, unpublished observations.
29. Assistance from H. Jo and R. Nissen in zebrafish studies and S. Bissonnette in MSC studies is gratefully acknowledged. This work was supported by NIH grants CA042063 to P.A.S., and GM60594 and GM68762 and a Burroughs-Wellcome Career Development Award to M.B.Y.

Formation of Regulatory Patterns During Signal Propagation in a Mammalian Cellular Network

Avi Ma'ayan,[1] Sherry L. Jenkins,[1] Susana Neves,[1] Anthony Hasseldine,[1] Elizabeth Grace,[1] Benjamin Dubin-Thaler,[3] Narat J. Eungdamrong,[1] Gehzi Weng,[1]* Prahlad T. Ram,[1]† J. Jeremy Rice,[4] Aaron Kershenbaum,[4] Gustavo A. Stolovitzky,[4] Robert D. Blitzer,[1,2] Ravi Iyengar[1]‡

We developed a model of 545 components (nodes) and 1259 interactions representing signaling pathways and cellular machines in the hippocampal CA1 neuron. Using graph theory methods, we analyzed ligand-induced signal flow through the system. Specification of input and output nodes allowed us to identify functional modules. Networking resulted in the emergence of regulatory motifs, such as positive and negative feedback and feedforward loops, that process information. Key regulators of plasticity were highly connected nodes required for the formation of regulatory motifs, indicating the potential importance of such motifs in determining cellular choices between homeostasis and plasticity.

A mammalian cell may be considered as a central signaling network connected to various cellular machines that are responsible for phenotypic functions (1). Cellular machines such as transcriptional, translational, motility, and secretory machinery can be represented as sets of interacting components that form functional local networks. The central signaling network that connects the various machine networks also receives and processes signals from extracellular entities such as hormones or neurotransmitters and ions. Experimental work has defined how different pathways interact to form networks and small-scale regulatory configurations such as switches (2, 3), gates (4, 5), feedback loops (6, 7), and feedforward motifs (8, 9) that decode signal duration and strength and process information. Identifying and characterizing regulatory motifs can move us from thinking about individual components to considering the functions of groups of components that act in a coordinated manner. Understanding how the functional organization of cellular systems changes in response to information flow is an important goal in systems biology. For systems containing many components, obtaining an overview of the patterns of regulatory motifs and defining their interrelationships can provide a format for in-depth analysis of individual units using quantitative biochemical representations.

From data in the experimental literature, we constructed a system of interacting cellular components involved in phenotypic behavior and used graph theory methods (10–12) to analyze qualitative relationships between nodes (components) in a network. In signaling networks, activation is achieved as a response to a stimulus. Information propagates through the system by a series of coupled biochemical reactions to regulate components responsible for cellular phenotypic functions. Here, we identify the regulatory features that emerge during such information flow in a simplified representation of a mammalian hippocampal CA1 neuron. Such neurons are capable of plasticity as defined by their ability to undergo long-term potentiation of synaptic responses (13, 14).

We represented the CA1 neuron as a set of interacting components that make up a network of signaling pathways that connects to various

Departments of ¹Pharmacology and Biological Chemistry and ²Psychiatry, Mount Sinai School of Medicine, New York, NY 10029, USA. ³Department of Biological Sciences, Columbia University, New York, NY 10029, USA. ⁴Functional Genomics and Systems Biology, IBM T. J. Watson Research Center, Yorktown Heights, NY 10598, USA.

*Present address: Scios Inc., 6500 Paseo Padre Parkway, Fremont, CA 94555, USA.
†Present address: Department of Molecular Therapeutics, M. D. Anderson Cancer Center, Houston, TX 77025, USA.
‡To whom correspondence should be addressed. E-mail: Ravi.Iyengar@mssm.edu
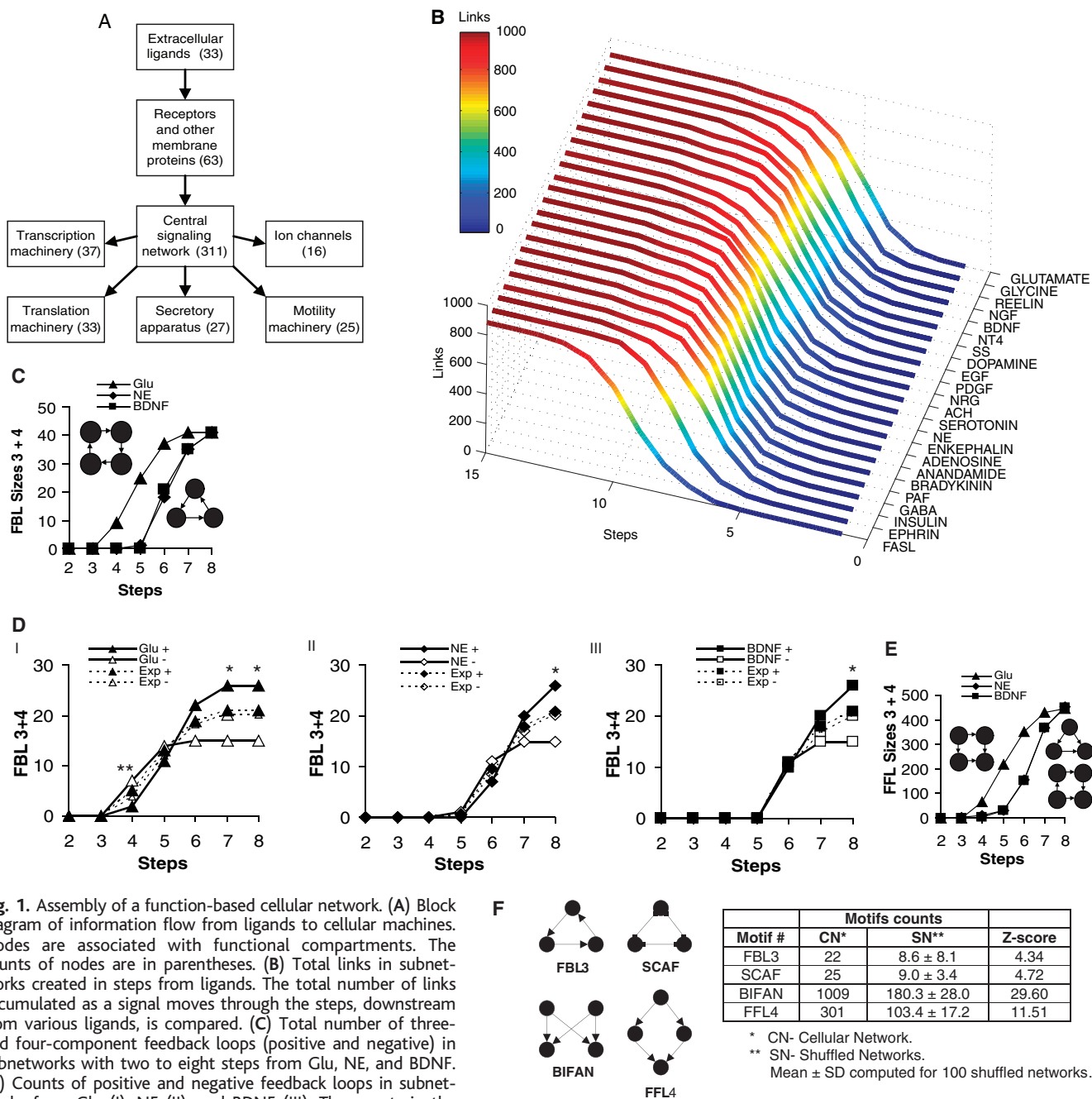
Fig. 1. Assembly of a function-based cellular network. (**A**) Block diagram of information flow from ligands to cellular machines. Nodes are associated with functional compartments. The counts of nodes are in parentheses. (**B**) Total links in subnetworks created in steps from ligands. The total number of links accumulated as a signal moves through the steps, downstream from various ligands, is compared. (**C**) Total number of three- and four-component feedback loops (positive and negative) in subnetworks with two to eight steps from Glu, NE, and BDNF. (**D**) Counts of positive and negative feedback loops in subnetworks from Glu (I), NE (II), and BDNF (III). The counts in the biological subnetworks (solid lines) are compared with the expected counts (dashed lines) developed using combinatorial probabilities for positive or negative feedback loops based on the number of total positive and negative links. ******, $P < .05$; *****, $P < .08$; binomial test. (**E**) Counts of three- and four-component feedforward motifs in subnetworks with two to eight steps from Glu, NE, and BDNF. (**F**) An abbreviated list of the motifs found in the fully connected network using the MFinder program (*19*). CN, cellular network; SN, shuffled networks; SNs were used as controls. Under SN, the mean and SD are given for motifs in 100 shuffled networks. See (*15*) for details.

cellular machines (Fig. 1A and fig. S1) (*15*). A fully connected network was constructed from direct interactions with functional effects documented in the experimental literature (fig. S2). We identified various regulatory motifs in the network. Some motifs were statistically enriched (*Z* test) compared with motifs found in shuffled networks with similar connectivity distribution (fig. S3 and table S1). We studied signal propagation resulting from ligand occupancy of receptors by building and analyzing a series of subnetworks that originate from nodes representing ligands. This is termed pseudodynamics because it represents propagation of reactions in chemical space rather than time series. Direct interaction between any two components, termed a link, consists of one or more underlying chemical reactions. Signal propagation from node to node is organized within the chemical space in units of steps. For any given node at step *n*, all immediate upstream nodes are at step *n*–1 and all nodes positioned one link downstream are at step *n*+1.

We counted the number of links per step as signals propagate from ligand-receptor interactions to their downstream effectors. The analysis of the emergent subnetworks for the different ligands showed a discernible pattern. For ligands that cause rapid, transient changes, such as glutamate and glycine, which regulate the Ca^{2+}-permeable *N*-methyl-D-aspartate (NMDA)–type glutamate receptor, early signal branching was
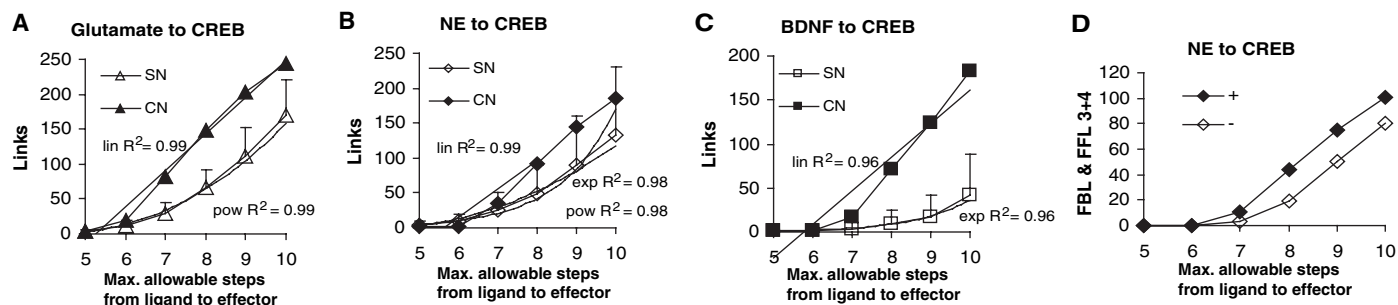
Fig. 2. Characteristics of subnetworks from three ligands to CREB. Subnetworks were analyzed starting from three extracellular ligands—glutamate, NE, and BDNF (source nodes)—extending to the transcription factor CREB (target node). (**A** to **C**) Changes in the number of links with increasing number of steps to reach the effectors. The same analysis was done with shuffled networks. Only the directionality of the links that do not involve the ligands or the effectors was randomly swapped while preserving the connectivity. The resultant graphs for both the cellular network (CN) and the shuffled networks (SN) were curve-fitted with Microsoft Excel. For all of the cellular subnetworks, the best fit function was linear (lin), R^2 = 0.96 to 0.99. For all of the shuffled networks, the best fit was obtained with exponential or power-law functions (exp or pow), R^2 = 0.96 to 0.99. (**D**) Counts of total three- and four-node positive and negative feedback and feedforward loops in subnetworks when different maximum numbers of steps are specified between NE and CREB.

extensive (that is, many links were formed in relatively few steps) (Fig. 1B). For ligands that cause permanent changes, such as FasL, which induces apoptosis, or ephrin, which alters neuronal morphology, there were fewer branches as the signal moved through the network. Between these extremes were many growth factors and ligands that bind G protein–coupled receptors (Fig. 1B). When the signal originating from any ligand had progressed through 15 steps, most of the network (nearly 1000 links) was engaged. This is a common property of large, highly connected directed graphs and in our case represents a very extensive propagation of the signal from the ligand analogous to prolonged receptor activation. For any individual ligand, the whole network was never fully affected, with a few nodes (usually other ligands) with single directed outgoing interactions not engaged. We characterized the network that emerged as signals were traced through each step from three ligands that are key regulators of plasticity in hippocampal neurons: glutamate (16), norepinephrine (NE) (17), and brain-derived neurotrophic factor (BDNF) (18). Glutamate influenced more links and nodes in early stages than did NE or BDNF, which showed similar profiles (fig. S4, A and B). The subnetwork characteristics were similar (fig. S4, C to E).

We analyzed the types of regulatory motifs formed as signals propagate from the ligands. A motif is a group of interacting components capable of signal processing. Motifs such as positive feedback loops promote the persistence of signals and serve as information storage devices (2), whereas negative loops limit signal propagation through the network. In counting these motifs, we used all possible configurations of loops with three and four components (Fig. 1C). In our model, glutamate activates 25 feedback loops within five steps, whereas NE and BDNF require six steps to recruit 20 feedback loops (Fig. 1C). We determined the relative abundances of negative and positive feedback loops as signal propagated from glutamate, NE, or BDNF (Fig. 1D). Using a

bionomial test and the combinatorial possibilities arising from the ratios of positive to negative links, it appeared that there were more than the expected number of negative feedback loops compared with positive feedback loops for glutamate at early steps ($P < 0.05$). This indicates that the early steps may have built-in controls to limit signal propagation. As the signal progressed to later steps, positive feedback loops tended to be more abundant than expected for all three ligands ($P < 0.08$). These profiles suggest that weak or short-lived signals may not penetrate into the network because of the early barrier posed by the abundance of negative feedback loops. However, as the number of steps increases and positive feedback loops appear to be more abundant, signals should persist and be able to evoke a biological response.
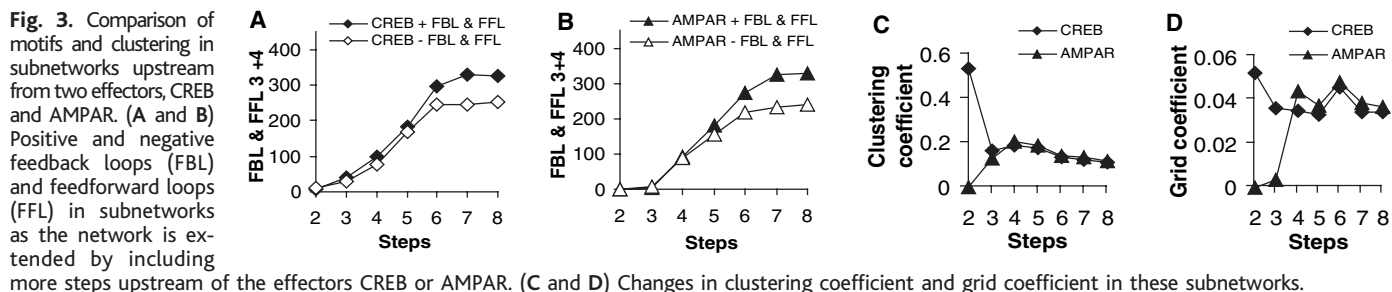
We also counted feedforward motifs (Fig. 1E and fig. S5), scaffolds (fig. S6A-I), and bifans (fig. S7B-I). Scaffold motifs are sets of three nodes connected through three neutral links. Their presence may indicate a mechanism for local clustering and may represent the basis for spatial specification of information flow. Feedforward loops are three- or four-component motifs in which the signal splits at a source node and consolidates at a target node. Feedforward loops can be either positive or negative (15). Positive feedforward loops provide two potential functions: a redundant set of pathways for information flow and an ability to extend the duration of activation or inhibition of the affected downstream component. When feedforward loops contain inhibitory links, they may function as gates (2). Bifans are four-component motifs in which two upstream components coregulate two downstream components (Fig. 1F) (19).

For each of these motifs, glutamate required fewer steps than did NE or BDNF to engage more motifs, although by step 8, when maximal connectivity is obtained, signals from the three ligands had spread to the same number of motifs (Fig. 1E and figs. S5 and S6). There was an increasing preponderance of positive over negative feedforward motifs for glutamate, NE, and

BDNF as the signal propagated through eight steps (fig. S5). The overall profile for any feedforward loops (positive or negative) was similar for all three ligands, although glutamate reached more feedforward loops in fewer steps. The bifan motifs were as abundant as feedforward loops and showed a similar pattern (fig. S6C).

In the CA1 neuron, signals from receptors affect major effectors such as the AMPA receptor channel (AMPAR), which regulates excitatory postsynaptic potentials, and the transcription factor cyclic adenosine monophosphate (cAMP) response element–binding protein (CREB), which regulates transcription. We analyzed a series of subnetworks that extend from glutamate, NE, and BDNF to these two effectors (figs. S7A and S8A) by varying the number of steps needed to reach the effectors from the ligand. The number of nodes engaged per step was nearly linear for all three ligands (Fig. 2, A to C). In contrast, when such pathways were tracked in subnetworks with randomly shuffled connectivity (15), the increase in links per step was best fit by either an exponential or a power-law function, suggesting that the binary interactions within the cellular system may be specified to provide preferential routes to key effectors that define the phenotype of the cell. Analysis of these subnetworks (15) indicated that even the most highly connected nodes only used some of their links to function within the preferred paths. Looking for the shortest paths from an input node (a ligand such as NE) to an output node (an effector such as CREB) allowed us to identify functional modules defined here as a set of interactions that may carry out a specific function and act semi-independently from other functional modules. Further refinement by inclusion of spatial specification and temporal dynamics is needed to define such modules rigorously.

The counts of regulatory motifs formed within the subnetworks, as signal propagates were nearly linear for both the positive and negative motifs. For glutamate and BDNF in the subnetworks leading to CREB, the positive

Fig. 3. Comparison of motifs and clustering in subnetworks upstream from two effectors, CREB and AMPAR. (**A** and **B**) Positive and negative feedback loops (FBL) and feedforward loops (FFL) in subnetworks as the network is extended by including more steps upstream of the effectors CREB or AMPAR. (**C** and **D**) Changes in clustering coefficient and grid coefficient in these subnetworks.

and negative motifs were evenly balanced through nine steps (fig. S8, A and B). Such balance of regulatory loops might explain how homeostasis is achieved even when a perturbing signal propagates through the system. Positive feedback and feedforward loops were more abundant than negative loops in the subnetworks from NE to CREB (Fig. 2D). This may allow the subnetworks to persistently hold and transfer information causing long-term changes. Such configurations of motifs may provide a systems-level explanation of why the cAMP pathway is associated with the late phase of long-term potentiation (LTP) in the CA1 neuron (*20–22*). Similar patterns of positive to negative motifs were observed for signal propagation from NE to AMPAR (fig. S9F). Patterns from glutamate and BDNF to AMPAR were also similar to that seen in subnetworks to CREB (fig. S9, E and G).

To analyze the subnetworks upstream of the two key effectors CREB and AMPAR, we used these effectors as source nodes and expanded the network in a stepwise manner, tracing the signals that feed into CREB and AMPAR. The number of positive and negative feedback loops converging on CREB and AMPAR were equal up to four steps upstream of the effector (Fig. 3, A and B). However, we found distinct patterns of clustering. Two steps above CREB, a high (0.53) clustering coefficient was observed. Clustering coefficients measure the abundance of three component motifs and thus indicate local connectivity density. By three or four steps upstream, for both CREB and AMPAR, the clustering coefficients were both above the average observed clustering for the entire network (0.2 versus 0.11) (Fig. 3C). The grid coefficients [extensions of the clustering coefficient that also consider rectangles (*23*)] for the subnetworks two to four steps upstream of CREB and AMPAR were also higher than that observed for the network as a whole (0.053 to 0.031 versus 0.026) (Fig. 3D). Extensive local communication between nodes upstream of key effectors may provide homeostatic regulation of these effectors.

To evaluate the role of the highly connected nodes, we analyzed a series of subnetworks generated by the progressive inclusion of nodes with higher connectivities. We started with a sparse network in which we included only nodes with four or fewer links. We measured the number of islands (isolated clusters of nodes that
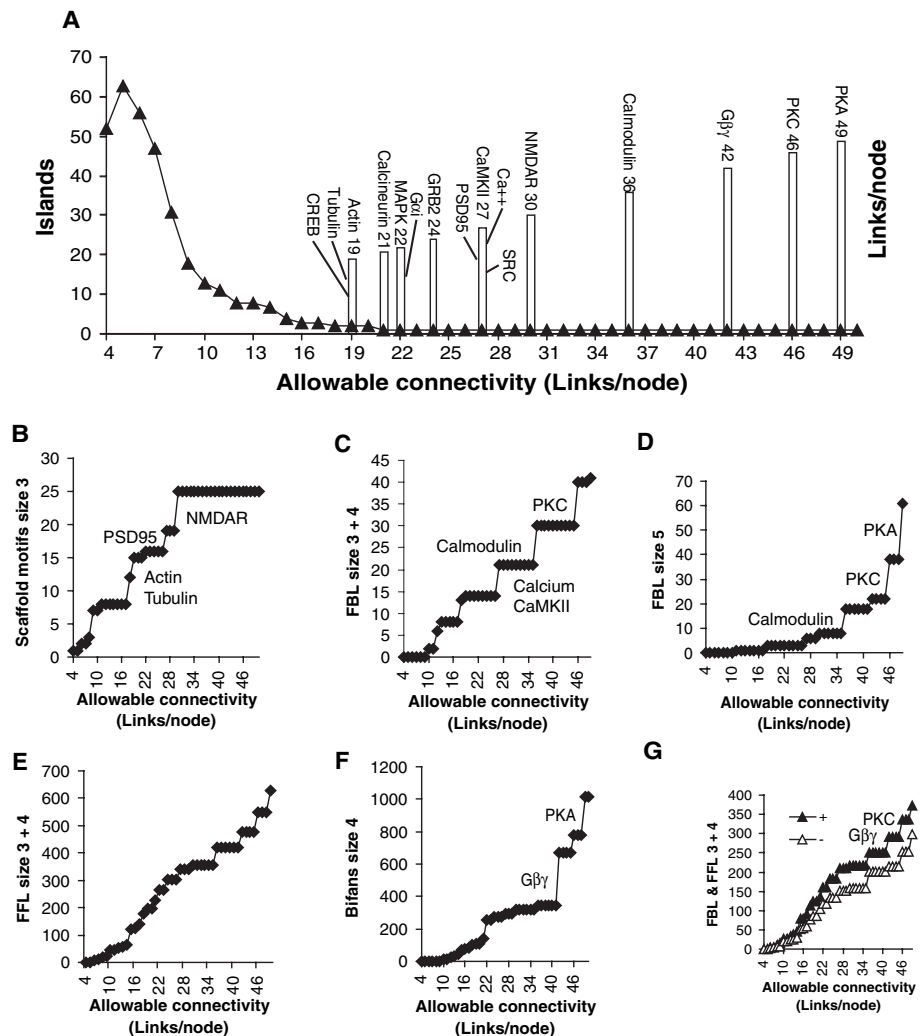
Fig. 4. Analysis of subnetworks with sequential incorporation of nodes with increasing connectivity. (**A**) Islands (isolated clusters of connected nodes) are plotted as a function of connectivity per node. A single network (one island) is formed when the nodes with 21 or fewer connections are included. All highly connected nodes starting at 19 links per node are shown. Single isolated nodes were not considered islands. (**B** to **F**) The number of motifs in the subnetworks created with nodes with different connectivity. Nodes that contribute disproportionately to the number of added motifs are listed next to the step they produce in the graph. (**G**) Counts of three- and four-component positive or negative feedback and feedforward loops are compared.

lack paths between them), clustering, characteristic path length, and number of motifs as we gradually added nodes with higher connectivity (fig. S10, A and B). The system was initially highly fragmented (63 islands). When all of the nodes with up to 21 connections were included, the network became a single island (one net-

work) (Fig. 4A). At this point, the most highly connected nodes, many of which are crucial components for LTP in hippocampal neurons, were not included. The nodes with more than 21 links per node included the four major protein kinases: mitogen-activated protein kinase (MAPK), calcium-calmodulin dependent protein

kinase II (CaMKII), protein kinase A (PKA), and protein kinase C (PKC) (Fig. 4A). Such highly connected nodes might contribute to regulatory motifs. Hence, we identified motifs that were formed if the highly connected nodes were included. The contributions of specific nodes to the formation of different motifs were readily discernable. Scaffolding motifs were largely dependent on the cytoskeletal proteins actin and tubulin, the synaptic scaffolding protein PSD-95, and NMDA receptors (Fig. 4B). Nearly 65% of the scaffolding motifs were formed without including enough nodes for the system to coalesce into a single island. In contrast, just 35% of the feedback and feedforward motifs and 20% of the bifan motifs were formed only in a network that included nodes with connectivity up to 21 links per node (Fig. 4, C to F). PKA and PKC appear to contribute to nearly 60% of the five-component feedback loops. Highly connected nodes, such as PKC, favored the emergence of positive motifs (Fig. 4D). These observations suggest that a function of these highly connected nodes may be to promote the formation of regulatory motifs that can allow for persistence of information and thus facilitate state change when appropriate external signals are received.

We developed maps to represent the pseudodynamic regulatory topology that our analyses had identified. We plotted the density of motifs at each step for the three ligands glutamate, NE, and BDNF by defining a "density of information processing" (DIP), which is the ratio of the additional new motifs (feedback loops, feedforward loops, and bifans) formed in each step to the increase in new links in each step (15) multiplied by the grid coefficient. This measure allowed us to identify the intensity and position in chemical space of information-processing activities. The DIP profile (Fig. 5A) at each step is plotted for the three different ligands through eight steps as signal propagates from receptors to cellular machines. Each DIP profile is distinctive, indicating that these represent differential stimulation of partially overlapping regions of the cellular network. Each ligand showed a "hot zone," where extensive information processing may occur. We also developed detailed maps to determine the position of the regulatory motifs in the chemical space of the network. For this, we specified the location of the nodes that participate in a motif between extracellular ligands and cellular machines on the basis of the shortest path lengths from the node within the motif to all extracellular ligands and to all components in the specified cellular machine. For each node, this yielded a "node location index" that measures the functional distance to each of the five cellular machines and to the ligands. We then identified the participation of these nodes in the various motifs. A parameter termed "motif location index" (MLI) was defined as the average of the location indices for the various nodes that comprise the motif in relation to the distance from the specified

machine (15). Five maps corresponding to the different cellular machines were generated (Fig. 5B). These maps indicate the location of the various regulatory motifs between extracellular ligands and cellular machines. Both common and distinctive features are observed. When pathways from ligands to each of the cellular machines were considered, a higher density of regulatory motifs was found at the middle of the maps (note the red band in each map), indicating that a major portion of the information processing occurs at the "center" of the network.

Distinct patterns of motifs were observed upstream of the different cellular machines. Directly upstream of the transcriptional machinery, feedforward motifs were abundant. In contrast, for the translational machinery, the regulation was more distal. For the secretory machinery, feedforward and feedback loops and scaffolds were found to be closer to the machine. For both the motility machinery and ion channels, regulation was largely concentrated in the center of the network (around MLI + 0.5). Some regulatory motifs are made of components within the cellular machines themselves.

This study provides an initial view of the regulatory capabilities that are formed as information flows through a cellular network. The overall profile of emergent motifs can be an indicator of the cell's information-processing capability. Here, organization is defined solely in terms of chemical space. It will be necessary to integrate this description with the physical
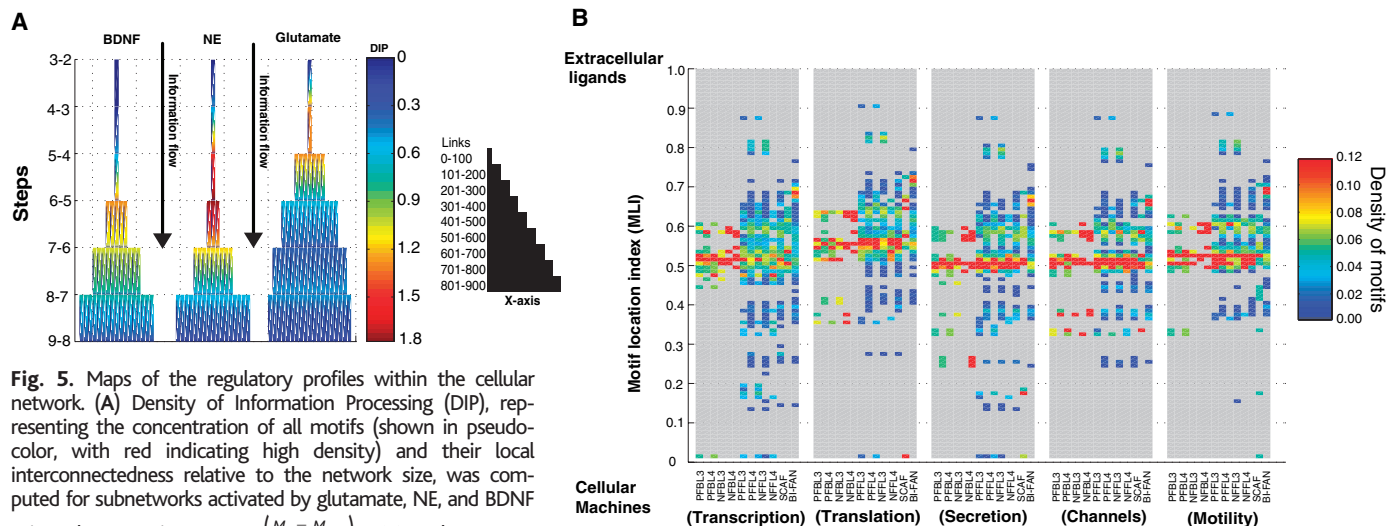
Fig. 5. Maps of the regulatory profiles within the cellular network. (**A**) Density of Information Processing (DIP), representing the concentration of all motifs (shown in pseudocolor, with red indicating high density) and their local interconnectedness relative to the network size, was computed for subnetworks activated by glutamate, NE, and BDNF using the equation $DIP_i = \left(\frac{M_i - M_{i-1}}{L_i - L_{i-1}}\right) \cdot GC_i$, where $M_i = FBL3_i + FBL4_i + FFL3_i + FFL4_i + BIFAN_i$. M_i is the total number of feedback loops, feedforward loops, and bifan motifs; L_i is the total number of links; and i is the step. FBL3 and FBL4 are feedback loops of size 3 and 4, FFL3 and FFL4 are feedforward loops of size 3 and 4, and BIFAN are bifan motifs of size 4. GC is the grid coefficient representing interconnectedness for the motifs, computed for the subnetwork at step i. DIP is plotted as a signal propagates vectorially through the network, as indicated by the downward arrow. The width of the bar represents the number of links engaged. (**B**) Relative distribution of regulatory motifs between ligands and cellular machines. Motifs were placed between extracellular ligands and cellular machines using the equation

$$MLI = \frac{\sum_{j=1}^{n} \left(\frac{CPLM_j}{CPLM_j + CPLL_j}\right)}{n}$$

where n is the size of the motif, CPLM is the characteristic

path length from a node within the motif to all other nodes in the cellular machine, and CPLL is the characteristic path length from a node to all extracellular ligands. If a node is an extracellular ligand, CPLL = 0 for that node; if the node is in the plasma membrane, CPLL = 1. If a node belongs to a cellular machine, CPLM = 0 for that node. The counts of motifs were placed in 100 bins based on the computed MLI and normalized to the fraction of total motifs for each class of motifs. An MLI value of 0 represents location at the cellular machines where all the nodes that make up the motif are within the cellular machine; a value of 1.0 represents location at the ligand level. PFBL and NFBL, three- and four-node positive and negative feedback loops, respectively; PFFL and NFFL, three- and four-node positive and negative feedforward loops; SCAF, three-node scaffold motifs; BIFAN, four-node bifan motifs. See (15) for details.

compartmentalization of components within the cell, and with temporal profiles of activation, to obtain a more comprehensive picture of the functional organization of a cell. Still, distance in chemical space (i.e., number of links between two distal nodes) is likely to be a major determinant of information processing that regulates phenotypic behavior.

The maps for individual ligands or cellular machines show distinct patterns of motifs. Combinations of ligands will likely produce many more patterns of connectivity. Thus, a cellular system may not be a single network but rather an ensemble of network configurations that are evoked by the stimuli-induced activation of various parts of the system. Identifying these network configurations and the functions they evoke is likely to provide more complete descriptions of how molecular interactions lead to cellular choices between homeostasis and plasticity.

References and Notes
1. J. D. Jordan, E. M. Landau, R. Iyengar, *Cell* **103**, 193 (2000).
2. U. S. Bhalla, R. Iyengar, *Science* **283**, 381 (1999).
3. U. S. Bhalla, P. T. Ram, R. Iyengar, *Science* **297**, 1018 (2002).
4. R. Iyengar, *Science* **271**, 461 (1996).
5. R. D. Blitzer *et al.*, *Science* **280**, 1940 (1998).
6. G. Lahav *et al.*, *Nat. Genet.* **36**, 147 (2004).
7. D. Angeli, J. E. Ferrell, E. D. Sontag, *Proc. Natl. Acad. Sci. U.S.A.* **101**, 1822 (2004).
8. S. Mangan, A. Zaslaver, U. Alon, *J. Mol. Biol.* **334**, 197 (2003).
9. S. Mangan, U. Alon, *Proc. Natl. Acad. Sci. U.S.A.* **100**, 11980 (2003).
10. D. J. Watts, S. H. Strogatz, *Nature* **393**, 440 (1998).
11. L. A. Amaral *et al.*, *Proc. Natl. Acad. Sci. U.S.A.* **97**, 11149 (2000).
12. A. L. Barabasi, R. Albert, *Science* **286**, 509 (1999).
13. T. V. Bliss, G. L. Collingridge, *Nature* **361**, 31 (1993).
14. S. A. Siegelbaum, E. R. Kandel, *Curr. Opin. Neurobiol.* **1**, 113 (1991).
15. Materials and methods are available as supporting material on *Science* Online.
16. O. Hvalby *et al.*, *Experientia* **43**, 599 (1987).
17. H. Katsuki, Y. Izumi, C. F. Zorumski, *J. Neurophysiol.* **77**, 3013 (1997).
18. H. Kang, E. M. Schuman, *Science* **267**, 1658 (1995).
19. N. Kashtan, S. Itzkovitz, R. Milo, U. Alon, *Bioinformatics* **20**, 1746 (2004).
20. P. V. Nguyen, T. Abel, E. R. Kandel, *Science* **265**, 1104 (1994).
21. R. Bourtchuladze *et al.*, *Cell* **79**, 59 (1994).
22. C. Pittenger, Y. Y. Huang, R. F. Paletzki *et al.*, *Neuron* **34**, 447 (2002).
23. G. Caldarelli *et al.*, *European Physical Journal B.* **38**, 183 (2004).
24. This research is supported by GM-54508 and GM-072853 from NIH and by an Advanced Research Center grant from the New York State Office of Science and Technology. A.M. is supported by Pharmacological Sciences Training grant GM-62754. S.N. is the recipient of an individual predoctoral National Research Service Award (GM-65065). R.D.B. is supported by National Institute on Drug Abuse grant DA15863. We thank B. Obrink, H. Dohlman, N. Hao, and J. Lisman for comments on the manuscript, M. Diverse-Pierluissi for help in identifying components of the secretory machine, S. Purushothaman for implementing the grid-coefficient function, and G. Kossinets (D. Watts laboratory, Columbia University, NY) for help with the initial analysis. Author contributions are described in the Supporting Online Material.

Containing Pandemic Influenza at the Source

Ira M. Longini Jr.,[1]* Azhar Nizam,[1] Shufu Xu,[1] Kumnuan Ungchusak,[2] Wanna Hanshaoworakul,[2] Derek A. T. Cummings,[3] M. Elizabeth Halloran[1]

Highly pathogenic avian influenza A (subtype H5N1) is threatening to cause a human pandemic of potentially devastating proportions. We used a stochastic influenza simulation model for rural Southeast Asia to investigate the effectiveness of targeted antiviral prophylaxis, quarantine, and pre-vaccination in containing an emerging influenza strain at the source. If the basic reproductive number (R_0) was below 1.60, our simulations showed that a prepared response with targeted antivirals would have a high probability of containing the disease. In that case, an antiviral agent stockpile on the order of 100,000 to 1 million courses for treatment and prophylaxis would be sufficient. If pre-vaccination occurred, then targeted antiviral prophylaxis could be effective for containing strains with an R_0 as high as 2.1. Combinations of targeted antiviral prophylaxis, pre-vaccination, and quarantine could contain strains with an R_0 as high as 2.4.

The world may be on the brink of an influenza pandemic (*1–4*). Avian influenza A (subtype H5N1) is causing widespread outbreaks among poultry in Southeast (SE) Asia, with sporadic transmission from birds to humans (*5*) and limited probable human-to-human transmission (*6*). Should an avian virus reassort with a human virus, such as influenza A subtype H3N2, within a dually infected human host or reassort in a nonhuman mammalian species, or if mutation of the virus occurs, the resulting new variant could be capable of sustained human-to-human transmission. The outbreak among humans would then spread worldwide via the global transportation network more rapidly than adequate supplies of vaccine matched to the new variant could be manufactured and distributed (*1, 7*). The pressing public health questions are whether and how we can contain the spread of an emerging strain at the source or at least slow the initial spread to give time for vaccine development. We used a discrete-time stochastic simulation model of influenza spread within a structured geographically distributed population of 500,000 people in SE Asia to compare the effectiveness of various intervention strategies against a new strain of influenza. Here we examine the effectiveness of the targeted use of influenza antiviral agents (*8–12*), quarantine, and pre-vaccination with a poorly matched, low-efficacy vaccine in containing the spread of the disease at the source.

We used information about rural SE Asia (*13, 14*) to construct the model population. Our goal was to represent the contact connectivity of a typical rural SE Asian population. The model population of 500,000 people was distributed across a space of 5625 km², yielding a density of 89/km², which is approximately the population density of rural SE Asia (*13*). The 500,000 people were partitioned into 36 geographic localities. This model is an extension of a model used to simulate interventions against pandemic influenza in the United States (*12*).

The model [see the supporting online material (SOM) for details] represents the number of close and casual contacts that a typical person makes in the course of a day. The age and household size distributions of the population are based on the Thai 2000 census (*13*). Many of the mixing group sizes and distributions are based on a social network study of the Nang Rong District in rural Thailand (*14*). We constructed the social network for contacts sufficient to transmit influenza as a large set of connected mixing groups. The close contact groups consist of households, household clusters, preschool groups, schools, and workplaces; and the casual contact groups consist of other social settings (such as markets, shops, and temples) and a single regional 40-bed hospital. All people can

[1]Department of Biostatistics, The Rollins School of Public Health, Emory University, 1518 Clifton Road, N.E., Atlanta, GA 30322, USA. [2]Ministry of Public Health, Nonthaburi, Thailand. [3]Department of International Health, The Bloomberg School of Public Health, Johns Hopkins University, Baltimore, MD, USA.

*To whom correspondence should be addressed. E-mail: longini@sph.emory.edu